Hydrogen dependence of the reaction mechanism and kinetics of water gas shift reaction on Ni catalyst: Experimental and DFT study

Tayyaba Noor[a,b,1], Yanying Qi [a,1] , De Chen[*a]

[a]Department of Chemical Engineering, Norwegian University of Science and Technology, Sem Sælands vei 4, Trondheim, NO-7491, Norway

[b] The present address: School of Chemical and Materials Engineering (SCME), National University of Sciences and Technology (NUST), H-12, Islamabad-44000, Pakistan

ABSTRACT: This paper presents a combined experimental and density functional theory study of the relative reactivity of surface species O*, OH*, and H* with CO* on nickel catalysts and their catalytic consequence in reaction mechanism and kinetics of water gas shift reaction. The kinetic study illustrated the hydrogen reaction order changes from 0.5 at relatively low hydrogen pressures to -1 at high hydrogen pressures. Detailed kinetic analysis indicated a hydrogen-induced change of the corresponding reaction pathway from hydrogen assisted CO activation to the redox mechanism with CO*+O* as a rate-determining step. The DFT investigation revealed that the surrounding surface H* atoms destabilize more significantly O* adsorption than H* adsorption, thus enhance more the reactivity of O* than H* towards reaction with CO at high H* coverage. This kinetic study provides an insightful depiction of the future study of CO activation on other transition metals and the catalyst development for WGS reaction.

KEYWORDS: Water-gas shift reaction, CO activation, Mechanism, kinetics, DFT, Nickel catalyst

Introduction

Hydrogen is a vital raw material in the chemical and petrochemical industries [1]. In the last few decades, there is an increasing demand for hydrogen, about annually 8-10% for chemical industries such as ammonia and methanol synthesis, oil refinery and biomass refinery as well as directly as fuel in fuel cells for transportation and power generation [2, 3]. H_2 can be practically produced from diverse resources, including fossil fuels such as coal and natural gas, biomass, and other renewable sources such as water by electrolysis process or using solar energy [4]. Steam reforming is the most prominent industrial method for hydrogen production, which accounts for about 80% of the total H_2 produced in the world. The steam methane reforming (SMR) process operates at high temperatures (800-950 °C), where the water gas shift (WGS) reaction is always accompanied to increase the yield of hydrogen from syngas (H_2 and CO) and CO_2 [5]. A typical composition of a reformer outlet syngas on a volume basis is 74% H_2, 18% CO, 6% CO_2, and 2% CH_4 [6, 7]. In a second stage, additional hydrogen is generated from syngas through the exothermic WGS reaction:

$$CO_{(g)} + H_2O_{(g)} \leftrightarrow H_{2(g)} + CO_{2(g)} \quad \Delta H^0 = -41.2 \text{ kJ mol}^{-1} \qquad (1)$$

The WGS reaction is an equilibrium exothermic reaction, which thermodynamically implies that decreasing temperature favors the conversion of carbon monoxide and steam towards hydrogen and carbon dioxide. This equilibrium condition is the major factor that the current industrial approach implements WGS in two stages. The high-temperature WGS reaction occurs at 300-500 °C using an iron-chromium oxide catalyst on alumina support [8-11] and reduces the exit CO concentration to about 3 vol% [12]. It is followed by a low temperature WGS reaction at 210-250 °C using a highly active copper zinc oxide catalyst on alumina support [10, 11] to reduce CO

concentration to 0.4 vol%. High purity H_2 up to 99.99% can be achievable by additional purification with e.g., a pressure swing adsorption unit. The overall process of hydrogen production from steam reforming demands high energy and cost [6, 7].

Reaction enhancement obtained by removing the generated H_2 by membrane reactor [13] or CO_2 from the reaction zone can serve the purpose of process simplification. Sorption-enhanced (SE) processes such as sorption-enhanced steam methane reforming (SESMR) reaction [14, 15] and sorption-enhanced water gas shift (SEWGS) reaction [16,17], are used to intensify the process by in-situ removal of CO_2 and thus shift the equilibrium towards hydrogen production. Nearly pure H_2 for fuel cell application can be produced by SEWGS [17] and SESMR of different oxygenated compounds such as ethanol [18, 19] and pure glycerol [20] as well as bio-syngas [21]. A catalyst with high activity is essential to the intensified production of the high purity of hydrogen in either SE processes or membrane reactors. The development of more active catalysts requires a better understanding of surface reactions on the catalyst surfaces.

The kinetics of WGS has been intensively studied experimentally, DFT, and microkinetic modeling, which has been reviewed by several researchers. [22-25] These studies extend over an extensive range in terms of catalyst or support type, operating temperature, pressure, and syngas composition. Almost similar kinetic expressions have been proposed for both the high-temperature and low-temperature catalysts. The kinetic models that have been approved by many authors from their experiments with various catalysts have been the Langmuir Hinshelwood model and the power-law model [26]. Recent publications use the kinetic expressions of Keiski et al. [27] and Hla et al. [28] for high-temperature WGS and Choi and co-workers [29] for low-temperature WGS. According to Fott et al. [30] over 20 different kinetic equations have been proposed, and there is still a lack of consensus over the nature and role of active sites and the reaction mechanism. The

difference in opinion on the nature of kinetics for the water gas shift reaction has been described due to the presence of impurities, mass transfer limitations, experiments carried out at atmospheric pressure, and the use of integral reactors for kinetic studies rather than the differential reactor [26][22]. Besides, Xu and Froment [31] have reported a reaction order of -1 for hydrogen for WGS on Ni/Al_2O_3. Hydrogen is the product of the WGS reaction, and the possible effects of hydrogen on the WGS kinetics have been often ignored. However, the kinetic consequence could have a profound implication on the reaction mechanism and kinetics of WGS. Several possible mechanisms, including redox mechanism, carboxyl, and formate pathways, have been proposed in the literature [23, 32]. Steady-state WGS kinetics suggested that a co-operative redox reaction mechanism could fit the kinetics [33]. Theoretical studies have been employed to investigate the WGS reaction mechanism on various metals, however, just a few focus on nickel catalyzed WGS, and there is still no agreement. The Ni/support interface is suggested to be the active site since it is a reservoir for reactive oxygenated species by Foppa et al. [34]. However, Ni (111) is suggested to be a better catalyst, which occurs by the carboxyl pathway with $CO + OH \rightarrow COOH$ as the rate-determining step in the study of Vlachos's group [32, 35]. Mohsenzadeh et al. reported that the redox pathway with $CO + O \rightarrow CO_2$ is the rate-determining step on Ni(111), Ni(100) and Ni(110) surface[36]. Zhou et al. proposed that the carboxyl pathway is favorable on clean Ni (111) surface and (211), while the redox pathway is preferred on Ni(100) [37, 38]. Therefore, the effect of hydrogen on WGS requires a detailed experimental and DFT investigation.

The present work deals with a combined experimental and DFT study of mechanism and kinetics of WGS at relatively high temperatures on the Ni catalyst, which is relevant for the pre-reforming of natural gas, steam reforming, and the sorption enhanced reforming processes. The aim of the present work is to elucidate the possible WGS reaction mechanism on nickel catalyst by a detailed

kinetic analysis in a wide range of operating conditions. Detailed kinetic study of WGS was performed, and measured rates were rigorously corrected for the distance from equilibrium in reforming reactions and for the number of exposed Ni surface atoms. The reaction order of CO, CO_2, H_2O, and H_2, and activation energy were measured. as well as the temperature on the reaction kinetic of WGS. The relevant reaction mechanism was ruled out by the combined kinetic analysis and DFT calculations.

Experimental

Hydrotalcite-like material (HT) has been used as the catalyst and was prepared by co-precipitation of salts $Ni(NO_3)_2 \cdot 6H_2O$, $Mg(NO_3)_3 \cdot 6H_2O$ and $Al(NO_3)_3 \cdot 9H_2O$. A stoichiometric ratio of cations was chosen to yield a 40 wt.% total metal loading of Ni. The precipitates obtained were then filtered and dried overnight at 70 ºC under vacuum. The catalyst was then calcined at 600 ºC for 6 hours in airflow to yield the 40 % Ni catalyst. The calcination temperature of 600 ºC was selected to suppress the formation spinel structure of $NiAl_2O_4$ and $NiMgO_2$. Finally, the calcined catalysts were pelletized, ground, and sieved to the desired particle size. A detailed description of the preparation of the precursor of these multifunctional catalysts used in the present work has been reported in the literature, and the catalyst characterization is published previously by He et al. [19].

The catalytic activity of prepared samples was examined in a tubular fixed-bed reactor. The kinetic experiments are conducted in an integrally fixed bed reactor with low mass and heat transport limitations and far from equilibrium conditions. The reactor used was made of quartz material with 8 mm internal diameter and 25 cm length. Catalyst weighing 4.8 mg and diluted with 40 mg of alpha-alumina was placed upon a porous plate of the fixed-bed reactor. A small amount

of alumina wool was used before and after the catalyst bed to minimize the catalyst particles sticking to the wall of the reactor. The unit used for conducting experiments of WGS was micro activity- reference reactor, from PID company, Spain. The schematic diagram of the reactor is shown in Figure 1 [17].

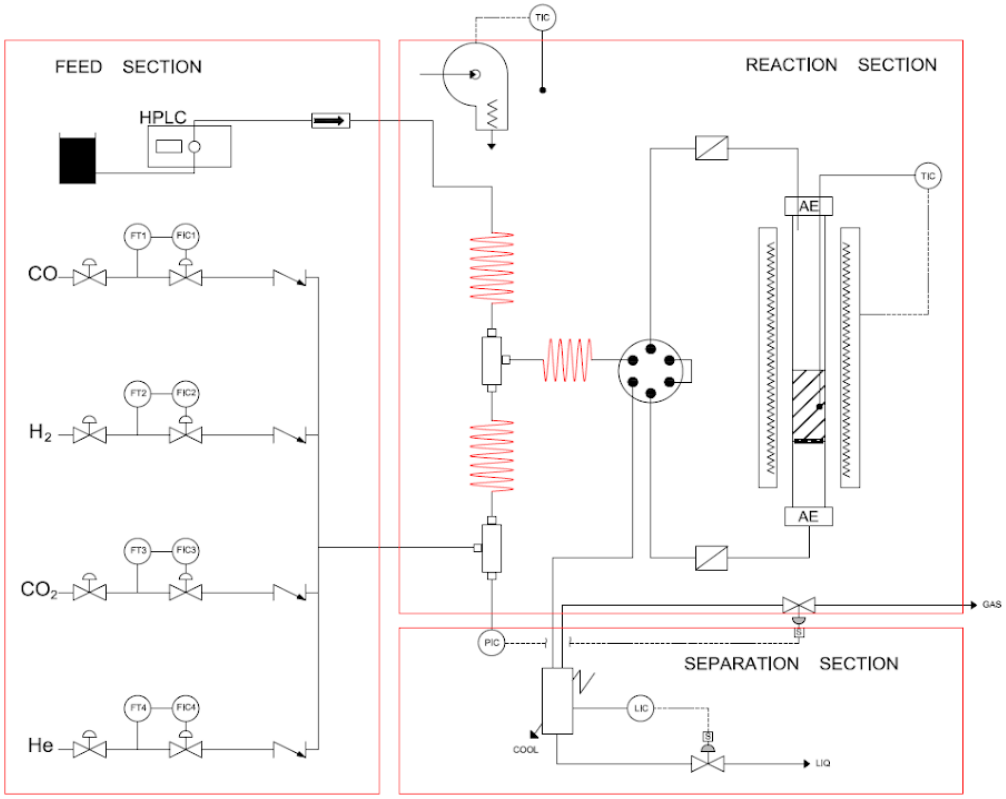

Figure 1: Schematic flow diagram of the experimental setup used for the kinetic study of WGS reaction

Before running the WGS experiments, the catalyst was activated via a reduction process in a mixed flow of 50% vol. H_2 and He at 670 ºC for 10 hours, using a heat rate of 5 ºC/min. 670 °C is needed to completely reduce the catalyst[17-19]. Thus, we performed the reduction process at 670 °C. Afterward, the catalyst bed was flushed with the inert gas flow while cooling to the desired reaction temperature. The temperature of the bed was monitored utilizing a thermocouple inserted

in the bed. The gases were introduced by the thermal mass flow controllers that have been calibrated using a soap bubble flow meter. The flow inside the reactor is up-down, whereby the reactant mixture is fed through the upper part of the reactor. Water was introduced into the reactor by using a Gilson HPLC pump and converted into steam using an evaporator inside the hotbox. The streams merge and flow to a 6-port valve that allows for selecting from two possible alternatives for the flow path: either towards the reactor or rerouting it towards the system's gas outlet (by-passing the reactor). At the reactor outlet, the effluent was directed to the liquid-gas separator, where condensation of liquids at low temperatures takes place. The liquid is continuously drained out of the reactor, whereby the gas flows to the outlet of the unit. A Gas Chromatograph (Agilent 3000 micro GC) equipped with a TCD detector along with Molsieve and a Plot U column was used to quantify all the components of the reactor effluent. An additional cold trap was placed before the products go to GC in order to completely remove any traces of moisture in the gas. The calibration of GC was performed by standard calibration gases, and the detection limit of this equipment for gas analysis is 0.001 vol.%. Steam to CO ratio was chosen to be 4 in order to minimize carbon deposition and methanation reaction. The conditions are modified to control the CO conversion under differential reaction conditions. Kinetic experiments were performed in an operational regime of low conversion (typically less than 25%) and far from equilibrium conditions to prevent the significant influence of gas products in backward reactions. The observed reaction rates are corrected for the approach to equilibrium. The reaction rate is calculated from conversion versus residence time data, using the equation 2 and is expressed in ($mol \cdot gcat^{-1} \cdot s^{-1}$), where x_{CO} is the conversion of CO in term of water gas shift activity, F_{CO} represent the inlet molar flow rate of CO and W_{cat} is the mass of catalyst. To exclude the effect of methanation activity, we use the conversion of CO to form CO_2, not the total conversion of CO.

The outlet of the reactor must not be at thermodynamic equilibrium. It was confirmed by calculating β using equation 3. It is the term reflecting the approach to equilibrium or the reverse reaction, so the forward reaction rate was corrected by the value of 1-β. K is the equilibrium constant for the WGS reaction and is given by equation 4 taken from the literature [39]. The turn over frequency (TOF) is calculated according to equation 5, where r is the reaction rate in ($mol \cdot gcat^{-1} \cdot s^{-1}$), D is the metallic dispersion of nickel, x_{Ni} represents the respective loading of Ni metal, and M is the molecule mass of Ni.

$$r = \left[\frac{x_{CO}}{W_{cat} / F_{CO}} \right] / (1 - \beta) \tag{2}$$

$$\beta = \frac{P_{CO_2} P_{H_2}}{K P_{CO} P_{H_2O}} \tag{3}$$

$$K = \exp\left(\frac{4577.8}{T} - 4.33 \right) \tag{4}$$

$$TOF = r * (M / x_{Ni} * D) \tag{5}$$

Computational methods

All the spin-polarized DFT calculations were performed in the Vienna Ab Initio Simulation Package (VASP) [40-42]. The nickel (111) surface was modeled by 3×3 unit cell of four layers and approximately 12 Å of vacuum spacing between the successive metal slabs. The top two layers were allowed to relax while the bottom two layers were fixed to their crystal positions with the experimental lattice parameter (3.52 Å). The Brillouin zone was sampled by 3×3×1 k-point Monkhorst-Pack grids, which was proved to be efficient for the cell [43]. RPBE has been proved to be more accurate than PW91 and PBE [44]. Therefore, the RPBE functional was utilized with the first order Methfessel-Paxton method for the electron smearing. The interactions between ion

cores and valence electrons were described by the projector augmented wave (PAW) method [45], with a plane wave energy cutoff of 400 eV. Calculations were converged until all forces on the atoms were lower than 0.01 eV/Å. Convergence tests of the calculation parameters were performed and also confirmed by the literature [43, 46].

The nudged elastic band (NEB) method [47] was used to locate the initial transition states by interpolating seven images between the initial and final states, which were subsequently optimized by using the dimer method [48]. The calculations were converged to within 1×10^{-7} eV/atom during the optimization. The maximum force in every degree of freedom is less than 0.01 eV/Å. The vibration frequencies were calculated to verify the transition states with one negative mode corresponds to the desired reaction coordinates.

Binding energy(E_{ads}) and activation energy(E_a) calculated as

$$E_{ads} = E_{A+slab} - E_A - E_{slab} \quad (6)$$

$$E_a = E_{TS} - E_{IS} \quad (7)$$

Where E_A is the total energy of the gas phase, E_{slab} is the total energy of the surface or the hydrogen pre-covered surface, and E_{A+slab} is the total energy of surface species on the slab，E_{TS} is the total energy of the transition state, and E_{IS} is the total energy of the reactants. Units of energies are eV. Activation energies of bimolecular surface reactions were calculated as the energy difference between the transition state and the reactant co-adsorbed on the surface

Results

The 40% Ni catalyst was synthesized using the co-precipitation method and was characterized by using XRD, SEM, BET, and hydrogen chemisorption techniques. The detailed characterization data are summarized in Table S1 in the supporting information. The Ni particle size is about 8.1 nm, which is rather close to the value measured by TEM (8.5 nm, Figure S2). The data obtained

are in good agreement to the one reported in the literature for the hydrotalcite catalyst [19]. The kinetic study of WGS has been performed on Ni catalyst in terms of the effects of the pressures of CO, CO_2, H_2O and H_2, as well as the temperature. The methane formation was observed at all conditions, but the selectivity of methane is relatively low.

Effect of CO and CO_2 pressures

The effect of CO and CO_2 partial pressure on the rate was investigated at 450 ^oC and total pressure of 1.5 bar with the constant partial pressure of H_2 (26.0 kPa) and H_2O (57.7 kPa). The experimental results for the relationship between TOF and CO partial pressure are plotted in Figure 2 (A) showed linear line, corresponding to the first-order dependence of reaction rate on CO concentration based on the line slope. From the point view of the Langmuir-Hinshelwood mechanism, it suggests that the adsorption of CO on the catalyst surfaces is relatively weak at the condition studied, which did not suppress the CO reaction.

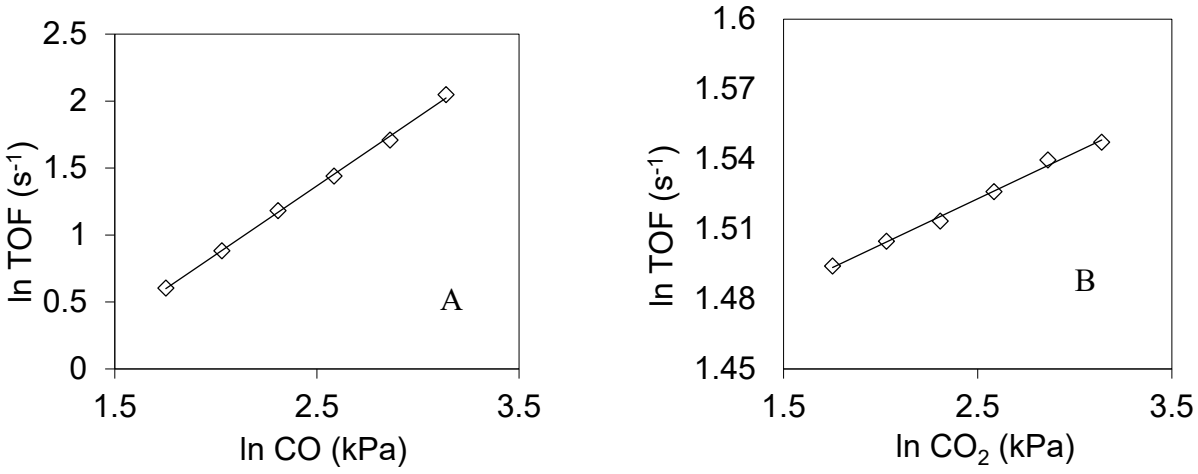

Figure 2. Dependence of reaction rate on CO (A) and CO_2 (B) partial pressure for 40%Ni, (450°C, 1.5 bar, 5.8-23.1 kPa CO, 57.7 kPa H_2O, 26.0 kPa H_2 and He as balance (A) 23.1 kPa CO_2, (B) 14.4 kPa CO).

Experimental data obtained in Figure 2 (B) implies a slightly positive dependence on carbon dioxide pressure under the reaction conditions investigated, corresponding to a reaction order close to zero for CO_2. It suggests that the adsorption of CO_2 on catalyst surfaces is possibly in equilibrium, which is not involved in the rate-determining steps.

Effect of hydrogen and steam pressures

Figure 3 (A) represents the TOF under different hydrogen partial pressure at a temperature of 450ºC. TOF increased initially and then decreased with H_2 pressure. There is an optimized hydrogen pressure corresponding to the maximum reaction rate at 14 kPa. The curve fitting provides 0.5 order at low hydrogen pressures and -1.0 at relatively high hydrogen pressures. Almost linear change of reaction rates with hydrogen pressure at both low and high hydrogen pressures, as well as a rapid change from positive effect to a negative effect of hydrogen, suggests a possible change in reaction mechanism with hydrogen pressure, which will be discussed in detail later.

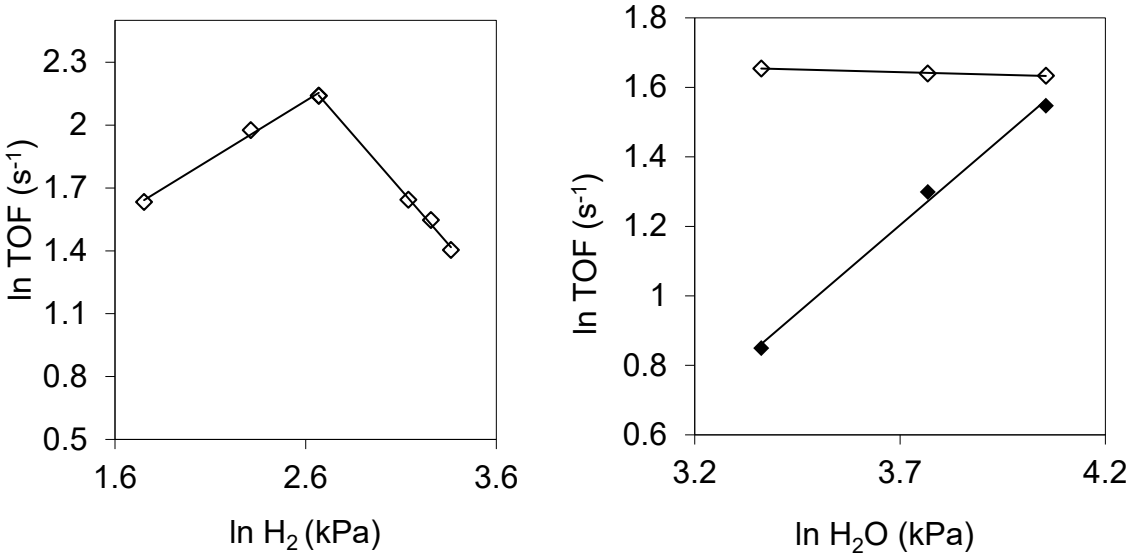

Figure 3. Reaction rate as a function of H_2 and H_2O partial pressure for 40%Ni, 450°C, 1.5 bar, 14.4 kPa CO, 23.1 kPa CO_2, He as balance (A) ◇ 5.8-31.7 kPa H_2 and 57.7 kPa H_2O (B) 28.8-57.7 kPa H_2O ◇ 5.8 kPa H_2 ◆ 26.0 kPa H_2,

The dependence of reaction rate on the partial pressure of water was examined over 40% Ni catalyst at low and high hydrogen pressures since the kinetic response of hydrogen pressure is different at low and high hydrogen pressures. The experimental results in Figure 3(B) indicate that the reaction rate increases linearly with increasing the partial pressure of water at high hydrogen pressure, while the reaction rate is independent of the water pressure at low hydrogen pressure. It clearly shows that the reaction order for water changes from zero to one from low hydrogen pressure to a high hydrogen pressure.

Effect of temperature

The effects of temperature on WGS reaction were investigated at relatively high hydrogen pressure (26kPa). The experimental results were expressed in the form of an Arrhenius plot (Figure 4). The activity of the catalyst follows Arrhenius like behavior, and the apparent activation energies were extracted from the slope of the curves. The reaction was studied at high temperatures (400-600^{o}C), and the forward reaction rates were used in the plots. Initially, forward reaction rates of catalyst increased with increasing temperature, consistent with Arrhenius type dependence, as shown in Figure 4. However, as the temperature range increases, a decrease in reaction rate was observed, opposite to the previously observed trend. The catalyst shows a maximum in a temperature range of 500-550 ^{o}C, after which the reaction rate starts to decrease. The activation energy (E_a) and the pre-exponential constant (k_o) values are summarized in Table 1, together with reaction orders.

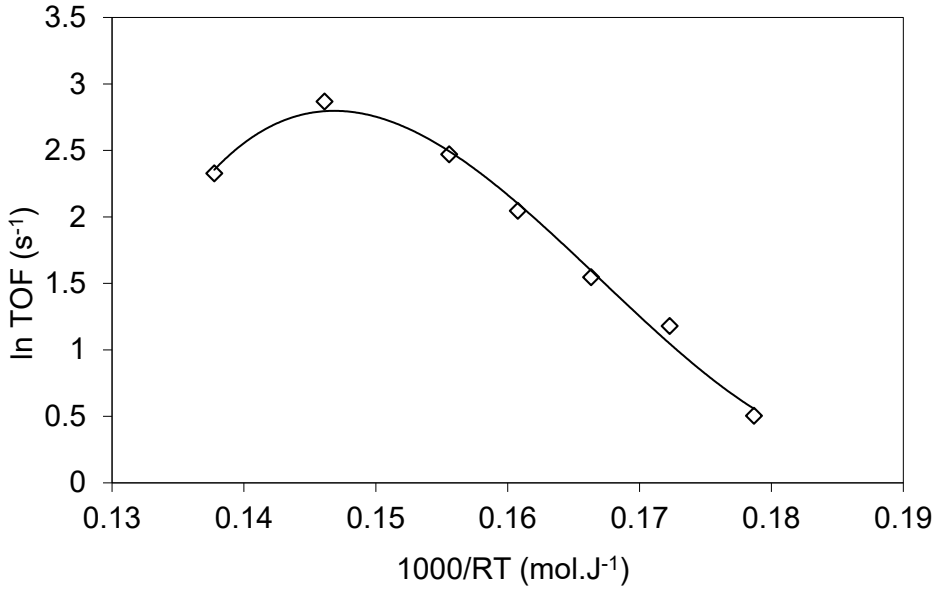

Figure 4. Arrhenius plot for 40 % Ni catalyst, 1.5 bar, 14.4 kPa CO, 57.7 kPa H_2O, 26.0 kPa H_2, 23.1 kPa CO_2, 28.8 kPa He, Temperature 400-600 °C

Table 1. Summary of observed reaction orders and activation energy for Ni- HT catalyst

Catalyst	Pre-exponential factor k_o (s^{-1} bar^{-1})	Activation Energy ($kJ \cdot mol^{-1}$)	H_2 Order		CO Order	CO_2 Order	H_2O Order		
			+ slope	- slope				Low P_{H_2}	High P_{H_2}
40%Ni	5.49E+06	83.7	0.55	-1.07	1.04	0.03		-0.03	1.01

Discussions

Kinetic model

The kinetic expression is obtained for the forward WGS reaction at high H_2 pressures based on the above results:

$$r_f = k_H P_{CO} P_{H_2O} P_{H_2}^{-1} \quad (8)$$

Where $k_H = k_o \exp^{(-Ea/RT)}$

where k_0 and Ea are summarized in Table 1. The kinetic model is in good agreement with the kinetic model reported by Xu and Froment [31]. It should be pointed out that site vacancy is approximate to 1 in our model since we performed all experiments at relatively low pressures in order to elucidate the reaction mechanism. However, the effect of reactant adsorption such as CO, H_2, and H_2O on the site vacancy should be taken into account at high pressures [31].

The kinetic expression is obtained for the forward WGS reaction at low H_2 pressures:

$$r_f = k_L P_{CO} P_{H_2}^{0.5} \quad (9)$$

Where $k_L = k_o \exp^{(-Ea/RT)}$

The significant enhancement of WGS activity by hydrogen and the shift of kinetics with hydrogen pressure have been observed for the first time. It requires a detailed kinetic analysis combining with DFT investigation.

Reaction mechanisms and favorable reaction pathway

Four possible mechanisms have been proposed in the literature [23, 32, 49, 50], namely 1) the redox mechanism 2) the carboxyl mechanism 3) the mechanism with COH, and 4) the formate mechanism. They are summarized in Table 2.

In the regenerative mechanism, also known as the redox mechanism, the oxidation-reduction cycle occurring on the catalyst surface is responsible for the reaction. This mechanism implies successive oxidation by adsorbed oxygen from H_2O and reduction of the reactive catalyst surface by CO. It is proposed that the catalyst surface is oxidized by water producing hydrogen, followed by reduction of the surface to convert CO to CO_2. The redox mechanism is mostly used to explain high-temperature WGS reaction, whereas the low-temperature shift reaction is commonly

explained by both redox and associate mechanism. Theoretical calculation suggested that the carboxyl mechanism and the formate mechanism is favorable [32].

Table 2. Possible reaction mechanism of water gas shift reaction

(1) CO + * ↔ CO*			
(2) H_2O + * ↔ H_2O*			
(3) H_2O* + * ↔ OH* + H*			
a) Redox Mechanism	**b) Carboxyl Mechanism**	**c) Mechanism with COH**	**d) Formate Mechanism**
(4) OH* + * ↔ O* + H*	(4) CO* + OH* ↔ COOH* + *	(4) OH* + * ↔ O* + H*	(4) OH* + * ↔ O* + H*
(5) CO* + O* ↔ CO_2* + *	(5) COOH* + * ↔ H* + CO_2*	(5) CO* + H* ↔ COH* + *	(5) CO* + H* ↔ HCO* + *
(6) CO_2* ↔ CO_2 + *	(6) CO_2* ↔ CO_2 + *	(6) COH* + O* ↔ COOH* + *	(6) HCO* + O* ↔ HCOO* + *
(7) 2H* ↔ H_2 + 2*	(7) 2H* ↔ H_2 + 2*	(7) COOH* + * ↔ H* + CO_2*	(7) HCOO* + * ↔ CO_2* + H*
		(8) CO_2* ↔ CO_2 + *	(8) CO_2* ↔ CO_2 + *
		(9) 2H* ↔ H_2 + 2*	(9) 2H* ↔ H_2 + 2*

The first three elementary steps such as CO and H_2O adsorption and dissociation of adsorbed H_2O are common. The different reaction mechanisms differ from the activation mechanism of CO at the reaction conditions, namely activation by O*, OH* and H*, respectively, which is schematically illustrated in a graphic tree plot (Scheme1). The activation energy for each elementary reaction from DFT calculations are also presented in Figure 5. The activation energies for the CO activation steps were taken from our previous work [43], while the activation energies for the steps related to reactions of CHO and COH were taken from the literature [32].

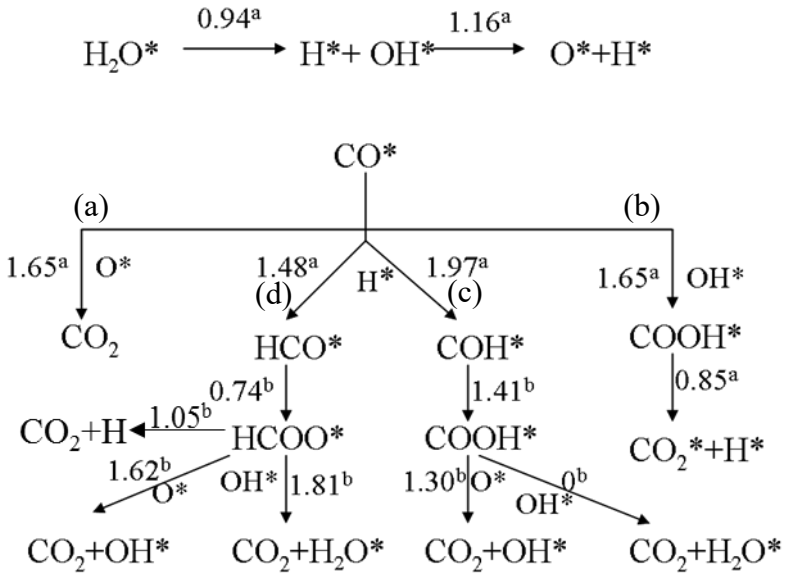

Figure 5. Schematic show of the activation energy of every elementary step. a is from literature using VASP [43]. b is from the literature using SIESTA software [32]. They all were calculated on a clean surface. The unit is eV.

The favorable reaction pathways for the WGS reaction depend on the relative reactivity of O*, OH*, and H* reacting with CO*. The DFT results suggested that the activation of CO* with H* (CO*+H* →HCO*) has the lower activation energy (1.48 eV) than the one of the activations by OH* and O* (1.65 eV). Moreover, the reaction steps of HCO* via oxidation to HCOO (0.74 eV) following decomposition to CO_2* and H* (1.05 eV) are more energetic favorable compared to the route via COH*. Another two pathways for CO_2 formation from HCOO*, O*- assisted route (1.62 eV) and OH*- assisted route (1.81 eV), have much more activation energy compared to the direct decomposition of HCOO* (1.05 eV). Therefore, the results in Figure 5 point out that the reaction pathway via HCO* and decomposition of HCOO* is the most energetic favorable one, where hydrogen assisted CO activation step could be the rate-determining step.

Although the reaction mechanism cannot be determined by kinetic modeling alone, kinetic modeling can often provide mechanistically rich information. The Langmuir-Hinshelwood rate expressions for each reaction mechanism were derived by the assumption of various rate-determining steps. The kinetic expressions are summarized in Table 3. The rate expression with the formate mechanism(d) is identical to the mechanism with COH(c) since the isomers (i.e., HCO and COH, as well as HCOO and COOH) cannot be discriminated in the kinetic expression. Based on the experimental results of zero-order for CO_2 (Table 1), the CO_2 desorption step was not assumed as the rate-determining in Table 3.

Table 3. The Langmuir-Hinshelwood rate expressions of the forward reactions for the four mechanisms (Table 2) with the assumed rate-determining steps and the corresponding reaction orders at low site coverages

Mechanism	[a]rds	Kinetic equation	H_2 order	CO order	H_2O order
a)	(3)	$r_2 = \frac{K_{Ia}P_{H_2O}}{\left(1+\sqrt{\frac{P_{H_2}}{K_7}}+K_2P_{H_2O}+\frac{P_{CO_2}\sqrt{P_{H_2}}}{K_1K_4K_5K_6\sqrt{K_7}P_{CO}}\right)^2}$	0	0	1
	(4)	$r_4 = \frac{K_{IIa}P_{H_2O}P_{H_2}^{-0.5}}{\left(1+K_2P_{H_2O}+\sqrt{\frac{P_{H_2}}{K_7}}+\frac{K_3K_2\sqrt{K_7}P_{H_2O}}{\sqrt{P_{H_2}}}\right)^2}$	-0.5	0	1
	(5)	$r_5 = \frac{K_{IIIa}P_{CO}P_{H_2O}P_{H_2}^{-1}}{\left(1+K_1P_{CO}+K_2P_{H_2O}+\frac{K_2K_3K_4K_7P_{H_2O}}{P_{H_2}}+\frac{K_3K_2\sqrt{K_7}P_{H_2O}}{\sqrt{P_{H_2}}}\right)^2}$	-1	1	1
b)	(3)	$r_3 = \frac{K_{Ib}P_{H_2O}}{\left(1+\sqrt{\frac{P_{H_2}}{K_7}}+K_2P_{H_2O}\right)^2}$	0	0	1
	(4)	$r_4 = \frac{K_{IIb}P_{CO}P_{H_2O}P_{H_2}^{-0.5}}{\left(1+K_1P_{CO}+K_2P_{H_2O}+\frac{K_3K_2\sqrt{K_7}P_{H_2O}}{\sqrt{P_{H_2}}}\right)^2}$	-0.5	1	1

	(5)	$r_5 = \frac{K_{IIIb} P_{CO} P_{H_2O} P_{H_2}^{-0.5}}{\left(1 + K_1 P_{CO} + K_2 P_{H_2O} + \sqrt{\frac{P_{H_2}}{K_7}} + \frac{K_1 K_2 K_3 K_4 \sqrt{K_7} P_{H_2O} P_{CO}}{\sqrt{P_{H_2}}} + \frac{K_3 K_2 \sqrt{K_7} P_{H_2O}}{\sqrt{P_{H_2}}}\right)^2}$	-0.5	1	1
c)	(4)	$r_4 = \frac{K_{Ic} P_{H_2O} P_{H_2}^{-0.5}}{\left(1 + K_1 P_{CO} + K_2 P_{H_2O} + \sqrt{\frac{P_{H_2}}{K_9}} + \frac{K_3 K_2 \sqrt{K_9} P_{H_2O}}{\sqrt{P_{H_2}}}\right)^2}$	-0.5	0	1
	(5)	$r_5 = \frac{K_{IIc} P_{CO} P_{H_2}^{0.5}}{\left(1 + K_1 P_{CO} + K_2 P_{H_2O} + \sqrt{\frac{P_{H_2}}{K_9}} + \frac{K_3 K_2 \sqrt{K_9} P_{H_2O}}{\sqrt{P_{H_2}}}\right)^2}$	0.5	1	0
	(6)	$r_6 = \frac{K_{IIIc} P_{CO} P_{H_2O} P_{H_2}^{-0.5}}{\left(1 + K_1 P_{CO} + K_2 P_{H_2O} + \frac{K_2 K_3 K_9 K_4 P_{H_2O}}{P_{H_2}} + \frac{K_3 K_2 \sqrt{K_9} P_{H_2O}}{\sqrt{P_{H_2}}} + \frac{K_1 K_5 P_{CO} \sqrt{P_{H_2}}}{\sqrt{K_9}}\right)^2}$	-0.5	1	1
	(7)	$r_7 = \frac{K_{IVc} P_{CO} P_{H_2O} P_{H_2}^{-0.5}}{\left(1 + K_1 P_{CO} + K_2 P_{H_2O} + \frac{K_2 K_3 K_9 K_4 P_{H_2O}}{P_{H_2}} + \frac{K_3 K_2 \sqrt{K_9} P_{H_2O}}{\sqrt{P_{H_2}}} + \frac{K_1 K_5 P_{CO} \sqrt{P_{H_2}}}{\sqrt{K_9}} + \frac{K_6 K_1 K_5 K_4 K_3 K_2 \sqrt{K_9} P_{CO} P_{H_2O}}{\sqrt{P_{H_2}}}\right)^2}$	-0.5	1	1
d)	(4)	$r_4 = \frac{K_{Ic} P_{H_2O} P_{H_2}^{-0.5}}{\left(1 + K_1 P_{CO} + K_2 P_{H_2O} + \sqrt{\frac{P_{H_2}}{K_9}} + \frac{K_3 K_2 \sqrt{K_9} P_{H_2O}}{\sqrt{P_{H_2}}}\right)^2}$	-0.5	0	1
	(5)	$r_5 = \frac{K_{IIc} P_{CO} P_{H_2}^{0.5}}{\left(1 + K_1 P_{CO} + K_2 P_{H_2O} + \sqrt{\frac{P_{H_2}}{K_9}} + \frac{K_3 K_2 \sqrt{K_9} P_{H_2O}}{\sqrt{P_{H_2}}}\right)^2}$	0.5	1	0
	(6)	$r_6 = \frac{K_{IIIc} P_{CO} P_{H_2O} P_{H_2}^{-0.5}}{\left(1 + K_1 P_{CO} + K_2 P_{H_2O} + \frac{K_2 K_3 K_9 K_4 P_{H_2O}}{P_{H_2}} + \frac{K_3 K_2 \sqrt{K_9} P_{H_2O}}{\sqrt{P_{H_2}}} + \frac{K_1 K_5 P_{CO} \sqrt{P_{H_2}}}{\sqrt{K_9}}\right)^2}$	-0.5	1	1
	(7)	$r_7 = \frac{K_{IVc} P_{CO} P_{H_2O} P_{H_2}^{-0.5}}{\left(1 + K_1 P_{CO} + K_2 P_{H_2O} + \frac{K_2 K_3 K_9 K_4 P_{H_2O}}{P_{H_2}} + \frac{K_3 K_2 \sqrt{K_9} P_{H_2O}}{\sqrt{P_{H_2}}} + \frac{K_1 K_5 P_{CO} \sqrt{P_{H_2}}}{\sqrt{K_9}} + \frac{K_6 K_1 K_5 K_4 K_3 K_2 \sqrt{K_9} P_{CO} P_{H_2O}}{\sqrt{P_{H_2}}}\right)^2}$	-0.5	1	1

The most of rate expressions indicate the first order in respective to CO, which is consistent with the experimental results as listed in Table 1. In this regard, the redox mechanism with OH* or CO* oxidation with a CO reaction order of 0 can be ruled out.

The kinetic analysis (Table 3) suggests that the hydrogen reaction order is relatively sensitive to the reaction mechanism. At the low hydrogen pressures, the reaction orders of 0.5 and 0 were

observed experimentally for hydrogen and water, respectively. The kinetic expressions of c(5) and d(5) in Table 3 with the rate-determining step of hydrogen assisted CO activation (CO*+H*) fits best the experimental observation. It is impossible to distinguish the mechanism c and d based only on the kinetic modeling. However, with combined DFT and experimental results, it confirms the prediction from DFT for the favorable reaction pathway with HCO* and HCOO * and HCO* formation as the rate-determining step as discussed above. This observation is also found in the methanation of CO on Ni catalysts [51]. It rationalizes well the experimental observation that the reaction rate increases with increasing hydrogen pressure, or, more precisely, the available surface H* at relatively low hydrogen pressures (Figure 3).

It is interesting to note that the reaction order for hydrogen rapidly jumped from 0.5 to -1, while the order for water changed from 0 to 1 at a certain hydrogen pressure, which cannot be explained by the strong hydrogen adsorption at high hydrogen pressure. Indeed, it might suggest a change in reaction mechanism with increasing hydrogen pressure. Only one mechanism (a(5), in Table 3), namely redox mechanism, with the CO* activation with O* as the rate-determining step fits the experimental reaction order for H_2, CO, and H_2O order of -1, 1 and 1, respectively. In order to understand the underlying nature of the change of reaction mechanism, the possible effects of the H site coverage on the relative reactivity of O* and H* are then investigated by DFT in the next section.

DFT study of hydrogen dependence of the reactivity of H* and O* with CO*

Firstly, the hydrogen coverage effect on the binding energy of H*, CO*, and O* was calculated. The results are summarized in Table 4. It was found that the calculated values in the present work are comparable to the literature values. In addition, the forward activation energy ($E_{a,f}$) of CO*+H*→HCO* at the clean Ni (111) surface is 1.52 eV, which is comparable to the literature

value 1.48 eV [43]and slightly higher than the literature value of 1.35 eV [32]. The DFT used here provides a backward activation energy of 0.21 eV for the above step, which is in good agreement with the literature value of 0.20 eV [43] and 0.21 eV [46].

Table 4. Binding energy of the species on Ni (111)[32, 43, 46]

species	our results [eV]	previous results [eV]
H	-2.64	-2.64 [46], -2.77 [32], -2.81[43]
H-3H	-2.63	-1.57 [46], -2.09 [32], -1.92 [43]
H-5H	-2.62	
H-6H	-2.62	
CO	-1.54	
CO-3H	-1.50	-5.14 [46], -4.81 [32], -5.67 [43]
CO-5H	-1.50	
CO-6H	-1.31	
O	-5.13	
O-3H	-5.04	
O-5H	-4.77	
O-6H	-4.45	

Note: *-XH: X H atoms pre-adsorbed on Ni (111)

Results in Table 4 show that pre-adsorption of hydrogen atoms on 3×3 unit cell of Ni (111) does not change the H adsorption heat, slightly reduced CO adsorption heat (-0.23 eV) and significantly reduce the O adsorption heat (-0.68 eV) when six hydrogen atoms adsorb on the surface. The activation energies for CO* reaction with O* and H* were then calculated at the 3×3 unit cell with different number pre-adsorbed hydrogen atoms. The results are summarized in Table 5. It was found the activation energies changes largely until six hydrogen atoms adsorb on the surface.

Table 5. Activation energy with different number of pre-covered hydrogen atoms

step	3H pre-covered surface[eV]	5H pre-covered surface[eV]	6H pre-covered surface[eV]

CO*+O*→CO_2*	1.54	1.44	1.08
CO*+H*→COH*	--	--	1.88
CO*+H*→HCO*	1.51	1.41	1.18

It proves that the step of CO reacting with oxygen becomes preferred at high hydrogen coverage, compared to the steps of CO*+H*. The reactivity of O* towards reaction with CO becomes higher at 6/9 MLH (monolayer hydrogen), compared to the reactivity of H*. Two important conclusions emerge from this analysis. Firstly, DFT investigation evidenced that the relative reactivity of O* and H* with CO* depends on the H coverage. It qualitatively rationalizes the possible changes in the reaction mechanism with the hydrogen pressure. At lower H coverage, the step CO*+H* displays a lower barrier, according to Figure 5. The barriers of CO*+H* and CO*+ O* decrease with the accumulation of H on the surface, which are 1.18 eV and 1.08 eV at the surface with six hydrogen atoms. Secondly, it qualitatively supports the experimental observation of reaction orders at the higher hydrogen pressures with suggested redox mechanism with CO*+O* as the rate-determining step since the barrier of CO*+O* is 0.1 eV smaller than CO*+H*. The transition states are represented in Figure 6.

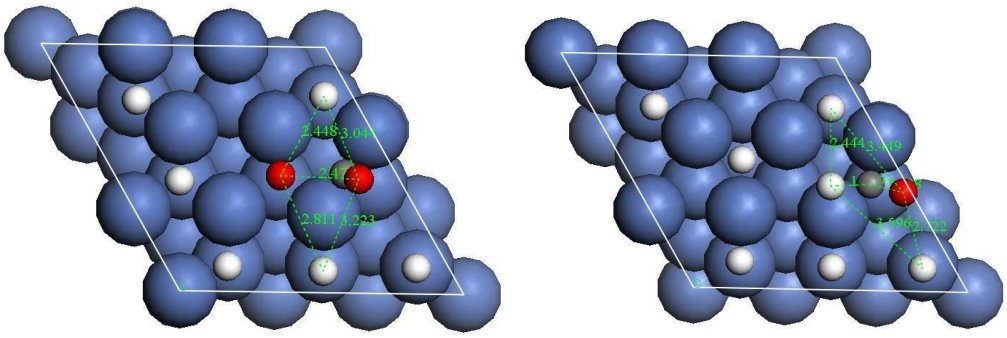

Figure 6. Top views of transition state: CO*+O*→ CO_2*(left), CO*+H*→HCO*(right).

The stability of O* on the Ni (111) has also been remarkably reduced by the co-absorbed hydrogen atoms surrounded in this reaction, which is similar with the previous study of the surface mobility of surface adsorbed O* on Pd (111) surface increased by co-adsorbed hydrogen [52]. The

co-adsorbed hydrogen atoms weaken the bond between oxygen and surface, which consequently makes O* more reactive and results in the proceeding of reaction through the redox mechanism at high hydrogen coverage. The observation is similar to the observation with reported on Cu catalysts, where the water gas shift reaction can proceed by several possible mechanisms depending upon the reaction conditions [53, 54].

Temperature dependence

The temperature dependence of the forward reaction rate is illustrated in Figure 4. The rate increased with increasing temperature at relatively low temperatures. However, the rate decreased with further increasing temperature. As the experiments were performed at high hydrogen pressures, and the redox mechanism was identified with the CO* activation with O* as the rate-determining step. The reaction rate can be expressed as:

$$r = k\theta_{CO*}\theta_{O*} \quad (10)$$

The surface O* is formed by the decomposition of H_2O. There are opposite effects of temperature on rate constant k and site coverage of CO* and H_2O* thus also O*, respectively. As expected, the rate constant k increases, while the site coverages of CO* and O* decrease with increasing temperature. Therefore the temperature dependence of the TOF appears a volcano curve. At the low temperatures, the increase in the rate constant with temperature is dominating. At high temperatures, the decrease in site coverage is prevailing, with further increasing temperature.

Conclusions

A cost-effective, non-precious metal-based nickel catalyst has been screened and found active for high-temperature water gas shift reaction. Combined DFT and experimental kinetic study

illustrated that the kinetics and reaction mechanism of WGS could change with the hydrogen pressure. The favorable reaction pathways depend on the relative reactivity of O*, H* and OH* on the Ni surfaces with CO*. The reaction order of H_2 and H_2O changed from 0.5 and 0 to -1 and 1 respectively, when the partial pressure of hydrogen increases. It corresponds to a shift of the reaction mechanism from hydrogen assisted CO activation to the redox mechanism. DFT investigation indicated that the surrounding adsorbed H (i.e., H*) much more significantly reduces the adsorption strength of O* compared to H* and CO*. Due to reduced stability of adsorbed O*, the CO*+O* reaction is more favorable compared to the reaction between CO* and H* at the high H* site coverage.

The work presented here will have a profound implication for the future study of reaction mechanism and kinetics of the reactions on transition metals as well as catalyst design, where catalyst properties and operating conditions could change the relative reactivity of the surface species. In addition, the present work will also have an important contribution to the process design to intensify the hydrogen production, such as membrane technology and sorption enhanced reforming or SEWGS.

Note:

1. T. N and Y. Q are considered equal first authors and have contributed equally to the paper.

Acknowledgments

The authors would like to acknowledge the financial support from the Research Council of Norway and iCSI center for Research-based Innovation. The computational time provided by the Notur project NN4685K is highly acknowledged. The authors would like to thanks Dr. Naseem

Iqbal from USPCAS-E, National University of Sciences and Technology (NUST), for the help in paper revision, and Dr. Jun Zhu from NTNU for the helps in experiments.

References

[1] R.D. Cortright, R.R. Davda, J.A. Dumesic, Hydrogen from catalytic reforming of biomass-derived hydrocarbons in liquid water, Nature, 418 (2002) 964-967.

[2] J.N. Armor, Catalysis and the hydrogen economy, Catal Lett, 101 (2005) 131-135.

[3] I. Dincer, C. Acar, Review and evaluation of hydrogen production methods for better sustainability, Int J Hydrogen Energ, 40 (2015) 11094-11111.

[4] J.D. Holladay, J. Hu, D.L. King, Y. Wang, An overview of hydrogen production technologies, Catal Today, 139 (2009) 244-260.

[5] Y. Zhang, C. Chen, X. Lin, D. Li, X. Chen, Y. Zhan, Q. Zheng, CuO/ZrO2 catalysts for water–gas shift reaction: Nature of catalytically active copper species, Int J Hydrogen Energ, 39 (2014) 3746-3754.

[6] M.A. Pen˜a, J.P. Gómez, J.L.G. Fierro, New catalytic routes for syngas and hydrogen production, Applied Catalysis A: General, 144 (1996) 7-57.

[7] I. Dybkjaer, Tubular reforming and autothermal reforming of natural gas — an overview of available processes, Fuel Process Technol, 42 (1995) 85-107.

[8] C. Rhodes, G.J. Hutchings, A.M. Ward, Water-gas shift reaction: finding the mechanistic boundary, Catal Today, 23 (1995) 43-58.

[9] V. Subramanian, D.-W. Jeong, W.-B. Han, W.-J. Jang, J.-O. Shim, J.W. Bae, H.-S. Roh, Rapid synthesis of magnetite catalysts incorporated with M (Cu, Ni, Zn, and Co) promoters for high temperature water gas shift reaction, New J Chem, 38 (2014) 4872-4878.

[10] S. Natesakhawat, X. Wang, L. Zhang, U.S. Ozkan, Development of chromium-free iron-based

catalysts for high-temperature water-gas shift reaction, J Mol Catal A-Chem, 260 (2006) 82-94.

[11] P. Kappen, J.-D. Grunwaldt, B.S. Hammershøi, L. Tröger, B.S. Clausen, The State of Cu Promoter Atoms in High-Temperature Shift Catalysts—An in Situ Fluorescence XAFS Study, J Catal, 198 (2001) 56-65.

[12] G.C. de Araújo, M. do Carmo Rangel, An environmental friendly dopant for the high-temperature shift catalysts, Catal Today, 62 (2000) 201-207.

[13] B.M. Castro-Domingues, P. Ivan; Ma, Liang-Chih; Ma, Rui; Dixon, G. Anthony; Kazantzis, K. Nikolaos; Ma, H. Yi, Integration of Methane Steam Reforming and Water Gas Shift Reaction in a Pd/Au/Pd-Based Catalytic Membrane Reactor for Process Intensification, Membranes, 6 (2016) 44-61.

[14] Y. Ding, E. Alpay, Adsorption-enhanced steam–methane reforming, Chem Eng Sci, 55 (2000) 3929-3940.

[15] J. Fermoso, F. Rubiera, D. Chen, Sorption enhanced catalytic steam gasification process: a direct route from lignocellulosic biomass to high purity hydrogen, Energ Environ Sci, 5 (2012) 6358-6367.

[16] C. Han, D.P. Harrison, Simultaneous shift reaction and carbon dioxide separation for the direct production of hydrogen, Chem Eng Sci, 49 (1994) 5875-5883.

[17] T. Noor, M.V. Gil, D. Chen, Production of fuel-cell grade hydrogen by sorption enhanced water gas shift reaction using Pd/Ni–Co catalysts, Appl Catal B-Environ, 150-151 (2014) 585-595.

[18] L. He, H. Berntsen, E. Ochoa-Fernández, J.C. Walmsley, E.A. Blekkan, D. Chen, Co–Ni Catalysts Derived from Hydrotalcite-Like Materials for Hydrogen Production by Ethanol Steam Reforming, Top Catal, 52 (2009) 206-217.

[19] L. He, H. Berntsen, D. Chen, Approaching Sustainable H2 Production: Sorption Enhanced

Steam Reforming of Ethanol, J Phys Chem A, 114 (2010) 3834-3844.

[20] L. He, J.M.S. Parra, E.A. Blekkan, D. Chen, Towards efficient hydrogen production from glycerol by sorption enhanced steam reforming, Energ Environ Sci, 3 (2010) 1046-1056.

[21] L. He, D. Chen, Single-stage production of highly concentrated hydrogen from biomass-derived syngas, Chemsuschem, 3 (2010) 1169-1171.

[22] W.F.Podolski, Y.G. Kim, Ind. Eng. Chem., Process Des. Develop., 13 (1974) 415-421.

[23] J. Ashok, M.H. Wai, S. Kawi, Nickel-based Catalysts for High-temperature Water Gas Shift Reaction-Methane Suppression, ChemCatChem, 10 (2018) 3927-3942.

[24] S. Saeidi, F. Fazlollahi, S. Najari, D. Iranshahi, J.J. Klemes, L.L. Baxter, Hydrogen production: Perspectives, separation with special emphasis on kinetics of WGS reaction: A state-of-the-art review, J Ind Eng Chem, 49 (2017) 1-25.

[25] M.H. Zhu, I.E. Wachs, Iron-Based Catalysts for the High-Temperature Water Gas Shift (HT-WGS) Reaction: A Review, Acs Catal, 6 (2016) 722-732.

[26] R.J.B. Smith, M. Loganathan, S. Shantha Murthy, A Review of the Water Gas Shift Reaction Kinetics, Int J Chem React Eng, 2010.

[27] R.L. Keiski, T. Salmi, P. Niemistö, J. Ainassaari, V.J. Pohjola, Stationary and transient kinetics of the high temperature water-gas shift reaction, Appl Catal A-Gen, 137 (1996) 349-370.

[28] S.S. Hla, D. Park, G.J. Duffy, J.H. Edwards, D.G. Roberts, A. Ilyushechkin, L.D. Morpeth, T. Nguyen, Kinetics of high-temperature water-gas shift reaction over two iron-based commercial catalysts using simulated coal-derived syngases, Chem Eng J, 146 (2009) 148-154.

[29] Y. Choi, H.G. Stenger, Water gas shift reaction kinetics and reactor modeling for fuel cell grade hydrogen, J Power Sources, 124 (2003) 432-439.

[30] P.Fott, J.Vosolsobe, V. Glaser, Kinetics of the carbon monoxide conversion with steam at

elevated pressures, Collect Czech Chem C, 44 (1979) 652-659.

[31] J. Xu, G.F. Froment, Methane steam reforming, methanation and water-gas shift: I. Intrinsic kinetics, Aiche J, 35 (1989) 88-96.

[32] R.C. Catapan, A.A.M. Oliveira, Y. Chen, D.G. Vlachos, DFT Study of the Water–Gas Shift Reaction and Coke Formation on Ni(111) and Ni(211) Surfaces, J Phys Chem C, 116 (2012) 20281-20291.

[33] Y. Li, Q. Fu, M. Flytzani-Stephanopoulos, Low-temperature water-gas shift reaction over Cu- and Ni-loaded cerium oxide catalysts, Appl Catal B-Environ, 27 (2000) 179-191.

[34] L. Foppa, T. Margossian, S.M. Kim, C. Müller, C. Copéret, K. Larmier, A. Comas-Vives, Contrasting the Role of Ni/Al_2O_3 Interfaces in Water–Gas Shift and Dry Reforming of Methane, J. Am. Chem. Soc., 139 (2017) 17128-17139.

[35] T.P. de Carvalho, R.C. Catapan, A.A.M. Oliveira, D.G. Vlachos, Microkinetic Modeling and Reduced Rate Expression of the Water–Gas Shift Reaction on Nickel, Ind Eng Chem Res, 57 (2018) 10269-10280.

[36] A. Mohsenzadeh, T. Richards, K. Bolton, DFT study of the water gas shift reaction on Ni(111), Ni(100) and Ni(110) surfaces, Surf Sci, 644 (2016) 53-63.

[37] M. Zhou, B. Liu, First-Principles Investigation of Adsorbate–Adsorbate Interactions on Ni(111), Ni(211), and Ni(100) Surfaces, Ind Eng Chem Res, 56 (2017) 5813-5820.

[38] M. Zhou, B. Liu, DFT Investigation on the Competition of the Water–Gas Shift Reaction Versus Methanation on Clean and Potassium-Modified Nickel(1 1 1) Surfaces, ChemCatChem, 7 (2015) 3928-3935.

[39] J.M. Moe, Design of Water-Gas Shift Reactions, Chem. Eng. Prog, 58 (1962) 33-36.

[40] G. Kresse, J. Furthmuller, Efficiency of ab-initio total energy calculations for metals and

semiconductors using a plane-wave basis set, Comput. Mater. Sci., 6 (1996) 15-50.

[41] G. Kresse, J. Hafner, Ab initio molecular dynamics for liquid metals, Phys Rev B, 47 (1993) 558-561.

[42] G. Kresse, J. Hafner, Ab initio molecular dynamics for open-shell transition metals, Phys Rev B, 48 (1993) 13115-13118.

[43] Y.-A. Zhu, Y.-C. Dai, D. Chen, W.-K. Yuan, First-principles calculations of CH4 dissociation on Ni(100) surface along different reaction pathways, J Mol Catal A-Chem, 264 (2007) 299-308.

[44] B. Hammer, L.B. Hansen, J.K. Norskov, Improved adsorption energetics within density-functional theory using revised Perdew-Burke-Ernzerhof functionals, Phys Rev B, 59 (1999) 7413-7421.

[45] P.E. Blochl, Projector Augmented-Wave Method, Phys Rev B, 50 (1994) 17953-17979.

[46] D.W. Blaylock, Y.-A. Zhu, W.H. Green, Computational Investigation of the Thermochemistry and Kinetics of Steam Methane Reforming Over a Multi-Faceted Nickel Catalyst, Top Catal, 54 (2011) 828.

[47] G. Henkelman, B.P. Uberuaga, H. Jónsson, A climbing image nudged elastic band method for finding saddle points and minimum energy paths, J Chem Phys, 113 (2000) 9901-9904.

[48] G. Henkelman, H. Jónsson, A dimer method for finding saddle points on high dimensional potential surfaces using only first derivatives, J Chem Phys, 111 (1999) 7010-7022.

[49] C.V. Ovesen, B.S. Clausen, B.S. Hammershøi, G. Steffensen, T. Askgaard, I. Chorkendorff, J.K. Nørskov, P.B. Rasmussen, P. Stoltze, P. Taylor, A Microkinetic Analysis of the Water–Gas Shift Reaction under Industrial Conditions, J Catal, 158 (1996) 170-180.

[50] K.C. Waugh, Prediction of global reaction kinetics by solution of the Arrhenius parameterised component elementary reactions: microkinetic analysis, Catal Today, 53 (1999) 161-176.

[51] M.P. Andersson, F. Abild-Pedersen, I.N. Remediakis, T. Bligaard, G. Jones, J. Engbæk, O. Lytken, S. Horch, J.H. Nielsen, J. Sehested, J.R. Rostrup-Nielsen, J.K. Nørskov, I. Chorkendorff, Structure sensitivity of the methanation reaction: H2-induced CO dissociation on nickel surfaces, J Catal, 255 (2008) 6-19.

[52] D.O. Demchenko, G.M. Sacha, M. Salmeron, L.W. Wang, Interactions of oxygen and hydrogen on Pd(111) surface, Surf Sci, 602 (2008) 2552-2557.

[53] M. J. Hong, N. Z. Ming, P. G. Xiang, X. Qian, Mechanism of the Copper-Catalyzed Water Gas Shift ReactionActa. Phys. Chim. Sin. 24 (2008) 2059-2064.

[54] A. A. Gokhale, J. A. Dumesic, M. Mavrikakis, On the Mechanism of Low-Temperature Water Gas Shift Reaction on CopperJ. Am. Chem. Soc. 130 (2008) 1402-1414.